

Micellar and Fractal Aggregates formed by two Triblock Terpolymers with different arrangements of one Charged, one Neutral Hydrophilic and one Hydrophobic Block

Aristeidis Papagiannopoulos^{*1}, Maria Karayianni¹, Grigoris Mountrichas¹, Stergios Pispas¹, Aurel Radulescu²

¹Theoretical and Physical Chemistry Institute, National Hellenic Research Foundation, 48 Vassileos Constantinou Avenue, 11635 Athens, Greece.

²Jülich Centre for Neutron Science JCNS Forschungszentrum Jülich GmbH, Outstation at Heinz Maier-Leibnitz Zentrum (MLZ), 1 Lichtenbergstraße, 85747 Garching, Germany.

Corresponding Author

* E-mail: apapagiannopoulos@eie.gr. Tel.: +30210-7273825. Fax: +30210-7273794

ABSTRACT

We have studied the self-assembled structures of two triblock amphiphilic polyelectrolytes of different topologies, containing a charged poly[sodium(sulfamate/carboxylate)isoprene] (SCPI) block, a polystyrene (PS) hydrophobic block and a hydrophilic neutral poly(ethylene oxide) (PEO) block in aqueous solutions, using Small Angle Neutron Scattering (SANS) and Light Scattering (LS). SANS reveals micellar and fractal aggregates in coexistence for both systems. In

the case of SCPI-b-PS-b-PEO there is a higher content in fractal aggregates in comparison with PS-b-SCPI-b-PEO. In both cases the micellar aggregates are stable under different solution conditions, whereas the fractal aggregates appear to break upon addition of salt in the PS-b-SCPI-b-PEO system. The detailed picture of the micellar aggregates is consistent with the anticipated morphology of charged and neutral spherical macromolecular brushes, extended to mixed and sequential brushes. The analytical description obtained by SANS is used to interpret the LS data which is very sensitive to the presence of two species and therefore provides information on average values of the measured parameters.

1. INTRODUCTION

Amphiphilic block copolymers, self-assembled in aqueous solutions, have been extensively studied as candidates for carriers in targeted drug delivery, bio-sensors, and tissue engineering[1]. Self-assembly of these macromolecular compounds leads to several geometries as core-shell micelles, vesicles, nanogels and aggregates depending not only on the chemistry of the monomeric units but also on external stimuli [1] as pH and salt content (for charged monomers) and temperature (for thermoresponsive blocks). Nanoparticles[2] with hydrophobic cores, and coronas made of water-soluble[3] (neutral micelles) or charged[4] macromolecular chains (polyelectrolyte micelles) provide a template for drug loading either on the hydrophobic core via hydrophobic interaction (in both cases) or via electrostatic attraction with the corona (in the case of polyelectrolyte micelles). Block copolymer topology is also influencing structure formation in such systems[5]. Charged or neutral nanogels[6] made of physically or chemically crosslinked macromolecules and polymeric aggregates[7] may also be utilized as pharmaceutical carriers.

Polyelectrolyte blocks included in self-assembled formations provide systems that can interact electrostatically with charged components in solution e.g. charged proteins or drugs. However they are highly responsive to stimuli as ionic strength and pH and in extreme cases they can be unstable [8]. On the other hand water soluble blocks are able to provide stability and solubility without the effect of ionic content. These features of the two separate systems and their individual advantages lead naturally to designing systems that combine their properties in a single system i.e. nano-formations containing both charged and neutral macromolecular blocks and to that purpose we have synthesized and studied triblock terpolymers that comprise of a hydrophobic block, a neutral water soluble block and a polyelectrolyte block in two different sequences employing anionic polymerization methodologies and recently established post-polymerization functionalization reactions [9].

In this study the aggregation of two triblock terpolymers, poly[sodium(sulfamate/carboxylate) isoprene]-b-polystyrene-b-polyethylene oxide (SCPI-b-PS-b-PEO) and polystyrene-b-poly[sodium(sulfamate/carboxylate) isoprene]-b-polyethylene oxide (PS-b-SCPI-b-PEO) in aqueous solutions was investigated by scattering techniques. Under several solution conditions micellar and fractal aggregates were found to co-exist in both systems by Small Angle Neutron Scattering. Light Scattering provided average (apparent) molecular weights and sizes that were in agreement with SANS data. This investigation highlights the sensitivity of aggregation on the several types of interactions between components in solution, the effects of macromolecular architecture on the structure of the aggregates and the ability of scattering techniques to characterize in detail these complex self-assembled structures non-invasively.

2. EXPERIMENTAL SECTION

2.1. Triblock Terpolymers Synthesis and Solutions Preparation

The triblock terpolymers poly[sodium(sulfamate/carboxylate) isoprene]-b-polystyrene-b-polyethylene oxide (SCPI₂₃₀-b-PS₅₂-b-PEO₁₅₁) from now on referred to as SCPI-b-PS-b-PEO and polystyrene-b-poly[sodium(sulfamate/carboxylate) isoprene]-b-polyethylene oxide (PS₄₁-b-SCPI₄₂₁-b-PEO₅₈₂) from now on referred to as PS-b-SCPI-b-PEO were synthesized by a combination of anionic polymerization and post polymerization functionalization reactions[9]. The subscripts in the blocks denote the polymerization degree of each block. The SCPI block consists of isoprene units that are randomly functionalized with hydrophilic sulfamate and carboxylate groups at a proportion of ca. 75%. It is an intrinsically flexible hydrophobic polymer that dissolves in water because of the dissociating units contained in its functionalized segments. In aqueous media SCPI has one strongly charged SO_3^- group (with Na^+ as a counterion) and a weak acidic COO^- group which is neutralized[9] by H^+ at pH below 4.2 (figure 1). Briefly the synthesis of the two triblock terpolymers was accomplished[10] as described below:

SCPI-b-PS-b-PEO synthesis: The synthesis of the triblock involve the anionic polymerization of a precursor triblock and the post polymerization functionalization of the polyisoprene block. The precursor polyisoprene-block-polystyrene-block-poly(ethylene oxide) (PI-PS-PEO) block copolymer was carried out by living anionic polymerization high vacuum techniques. Initially, isoprene was polymerized in benzene at room temperature, using sec-butyl lithium as initiator. Subsequently, a small amount of THF was added, followed by the addition of styrene at room temperature. Finally, phosphazine base and ethylene oxide were added and the temperature of the reaction mixture was raised to 40°C to polymerize the PEO block. The polymerization was terminated by addition of degassed methanol followed by two drops of concentrated HCl. At the end of each polymerization step, aliquots were isolated in order to control the success of the

polymerization. During the second step, i.e. the post polymerization reaction, a predetermined amount of polymer was placed in a two-necked 100 mL round bottom flask equipped with a septum. Carefully dried diethyl ether was distilled into the flask under vacuum and the copolymer was left to dissolve overnight (final copolymer concentration was $c = 50 \text{ g L}^{-1}$). Then, chlorosulfonyl isocyanate (CSI, from Acros) was added under N_2 dropwise, while the temperature was kept at $0 \text{ }^\circ\text{C}$. The reaction of the polymer with CSI was continued for 6 h at $0 \text{ }^\circ\text{C}$ in dark and in a stream of N_2 . It has to be noted that precipitation was observed after one hour of reaction. An amount of NaOH solution in water/methanol (1/3) was added dropwise. The diethyl ether was evaporated in vacuum and the remaining solution was refluxed overnight under N_2 . After the end of the reaction, the solvents were evaporated under vacuum and the solid was dialyzed against water.

PS-b-SCPI-b-PEO synthesis: A similar, to the case of SCPI-b-PS-b-PEO, procedure has been followed for the synthesis of the precursor polymer and the post polymerization reaction. The difference was the addition order of the monomers. This time polystyrene block was synthesized first, followed by the addition of isoprene, in the absence of THF.

The copolymers were characterized by size exclusion chromatography, $^1\text{H-NMR}$ and ATR-FTIR spectroscopy in order to determine their molecular characteristics.

In order to prepare aqueous solutions of mass concentration 1mg/ml , 30mg of a triblock terpolymer were stirred for 1 hour in 10ml of tetrahydrofuran (THF, from Fluka, UV spectroscopy grade) at 60°C . Subsequently, 30ml of D_2O or H_2O (for SANS or LS measurements respectively) was added dropwise under vigorous stirring. THF was subsequently removed by evaporation at $65 \text{ }^\circ\text{C}$ under stirring. NaCl was used as a salt and NaOH or HCl (NaOD or DCl in D_2O in order to minimize the incoherent scattering in SANS) for fixing the pH.

The contribution of the added acid or base to the ionic strength was about 10^{-4} M hence we refer to these solutions as solutions with no added salt. All sample solutions were filtered with $0.45\mu\text{m}$ PVDF membrane filters in order to remove any large aggregates or dust particles.

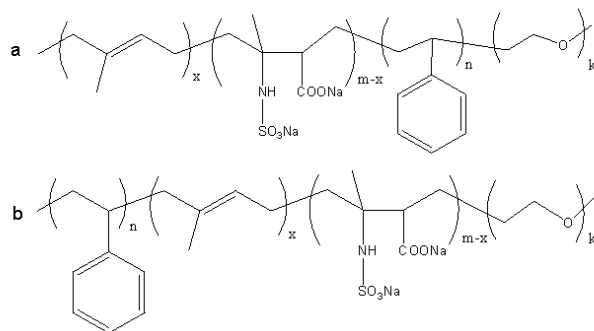


Figure 1: Molecular structures of the two triblock terpolymers used in this study. (a) SCPI-b-PS-b-PEO and (b) PS-b-SCPI-b-PEO.

2.2. Small Angle Neutron Scattering

Small Angle Neutron Scattering (SANS) experiments were performed on the KWS-2 high intensity/wide- q small angle neutron diffractometer, at the research reactor FRM II (Jülich Centre for Neutron Science). The nominal scattering vector (q) range is from 0.002 to 0.2 \AA^{-1} (real space length scales ~ 1000 to 10 \AA). This range was covered by three separate detection/neutron wavelength configurations. The high range was measured at 2m detection length with a 4.5 \AA wavelength and the intermediate and low q -ranges at 8m detection length with 4.5 \AA and 19 \AA neutron wavelengths respectively.

The SANS differential cross section is obtained by the scattered intensity $I(q)$ as a function of scattering wave-vector, $q = \frac{4\pi}{\lambda} \sin \frac{\theta}{2}$, where λ is the wavelength of the neutrons and θ is the

scattering angle. The scattered intensity is collected by a 2-D detector in the form of azimuthally isotropic patterns (normal for dilute solutions) which is afterwards azimuthally integrated leading to the 1-D intensity $I(q)$. The 2-D raw data are corrected for the scattering from the empty cell and the solvent, the electronic and background noise. Lupolen and plexiglass were used as standards to set the data to absolute scale.

In a SANS experiment the instrument's resolution function $\Delta q(q)$ has to be taken into account and consequently all the theoretically calculated scattered intensities $I^{th}(q)$ in this study are convoluted [11] by a Gaussian distribution function (equation 1). The convoluted curves $I^{conv}(q)$ are the ones fitted against the experimentally obtained data.

$$I^{conv}(q) = \frac{1}{\sqrt{2\pi}\Delta q(q)} \cdot \int_{-\infty}^{+\infty} dq' \cdot \exp\left(-\left(\frac{q'-q}{\sqrt{2}\Delta q(q)}\right)^2\right) \cdot I^{th}(q') \quad (1)$$

The instrument's resolution function $\Delta q(q)$ is given by $\Delta q(q) = (\Delta q_\lambda^2 + \Delta q_{geo}^2)^{1/2}$, where a q -dependent (Δq_λ) and a q -independent (Δq_{geo}) term are contained. The first term is connected to the wavelength spread ($\frac{\Delta q_\lambda}{q} = \frac{\Delta \lambda}{\lambda}$ with $\frac{\Delta \lambda}{\lambda} = 0.2$ for KWS-2) and the second term to the instrument configuration [12] which is defined by the source and sample apertures, the collimation drift line, the sample-to-detector distance, gravity and the detector resolution). More importantly, the instrument's resolution function, is experimentally determined by SANS on a model colloidal silica dispersion [12]. This system has sharp scattering features and its structural parameters have been previously determined by small angle X-ray scattering. So the experimentally determined resolution function is also checked by theoretical calculations based

on the instruments parameters [12]. In the “Results and Discussion” section theoretically calculated scattered intensities are denoted in short as $I(q)$ although the convoluted scattered intensity is fitted to the experimental data.

The temperature of the samples was set at 25 °C by a Julabo thermostat with an accuracy of 0.01°C.

2.3. Light Scattering

An ALV/CGS-3 compact goniometer system (ALV GmbH, Germany), equipped with a ALV-5000/EPP multi tau digital correlator and a He-Ne laser operating at the wavelength of 632.8 nm was used for the Light Scattering (LS) measurements. In Static Light Scattering (SLS) the Rayleigh ratio was calculated with respect to a toluene standard. SLS measurements were performed at a series of angles in the range 30-150°.

SLS data were treated [13] by the Zimm plot:

$$\frac{Kc}{R(q,c)} = \frac{1}{M_w P(q)} + 2A_2 c \quad (2)$$

where q is the scattering wave vector, M_w is the weight-averaged molar mass and A_2 the osmotic second virial coefficient of the particles in solution. $R(q, c)$ is the corrected Rayleigh ratio. $P(q)$ is the particle form factor, $P(q) = 1 - \frac{1}{3} q^2 R_{g,SLS}^2$, where $R_{g,SLS}^2$ the squared z-averaged radius of gyration. K is the contrast factor [14] for LS and depends on the refractive index increment of the scattering particles.

In Dynamic Light Scattering (DLS) the intensity auto-correlation functions $g^{(2)}(t)$ are collected [15] at different scattering angles (30-150°) and can be analysed by the CONTIN algorithm. The characteristic relaxation rate $\Gamma(q)$ is taken from the position of the maximum

($\tau(q)$) of the distribution function of relaxation times ($\Gamma(q) = \frac{1}{\tau(q)}$). In the case of diffusive modes there is a linear relation between $\Gamma(q)$ and q^2 i.e. $\Gamma(q) = D \cdot q^2$ and hence the diffusion coefficient D is obtained. The hydrodynamic radius, R_h , is extracted from the Stokes-Einstein equation (equation 3).

$$R_h = \frac{k_B T}{6\pi\eta D} \quad (3)$$

where η is the viscosity of the solvent, k_B is the Boltzmann constant and T is the absolute temperature. All the LS experiments were performed at 25 °C set by a PolyScience temperature controller.

3. RESULTS AND DISCUSSION

3.1. Modelling the SANS Data

Scattered intensities (I) as a function of scattering wave-vector (q) from SCPI-b-PS-b-PEO and PS-b-SCPI-b-PEO triblock copolymers are shown in figures 2 and 3 for all the solution conditions studied. The scattering profiles from SCPI-b-PS-b-PEO (figure 2) show weak while characteristic oscillations at the intermediate and the high q -range ($q \geq 0.02 \cdot \text{\AA}^{-1}$) whereas another kind of behavior is observed at low q . In this regime the scattering profile can be viewed as a quasi-plateau (at very low q) followed by a power-law (at higher q). The intermediate and high q -regimes indicate that objects of well-defined geometry are possibly observed which do not change significantly upon changing solution conditions i.e. the shape of the curves is virtually unchanged upon changing solution conditions (the curves collapse on a single master-curve in this regime after appropriate normalization, data not shown). The low q -regime indicates objects of fractal morphology[16] with radius of gyration higher than the one of the

objects of well-defined geometry. In this regime there is no collapse of the curves on the same master curve, when the intermediate and high- q regimes collapse on a single master curve after suitable normalization (as mentioned above). This means that changing solution conditions the relative contributions to the scattered intensity, by the two species, change. The situation is similar for the PS-*b*-SCPI-*b*-PEO triblock copolymer (figure 3). The fractal objects dominate the scattering up to $q \approx 0.02 \cdot \text{\AA}^{-1}$ as for the first system. At higher q -values there is a single bump which indicates a characteristic oscillation.

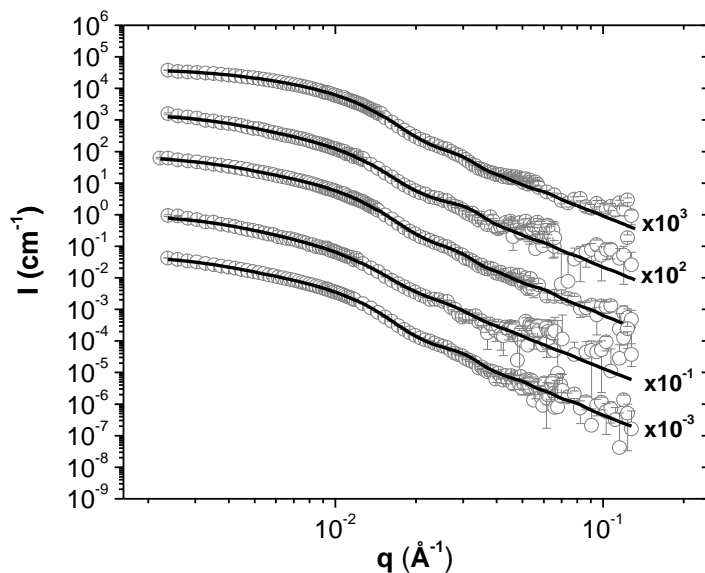


Figure 2: SANS intensities from SCPI-*b*-PS-*b*-PEO 1mg/ml in aqueous solutions of different conditions. From top to bottom: pH3/0M NaCl, pH7/0M NaCl, pH9/0M NaCl, pH7/0.1M NaCl and pH7/0.5M NaCl. Multiplication factors (as pointed in the figure) have been used for sake of clarity. The lines are fits to the experimental data.

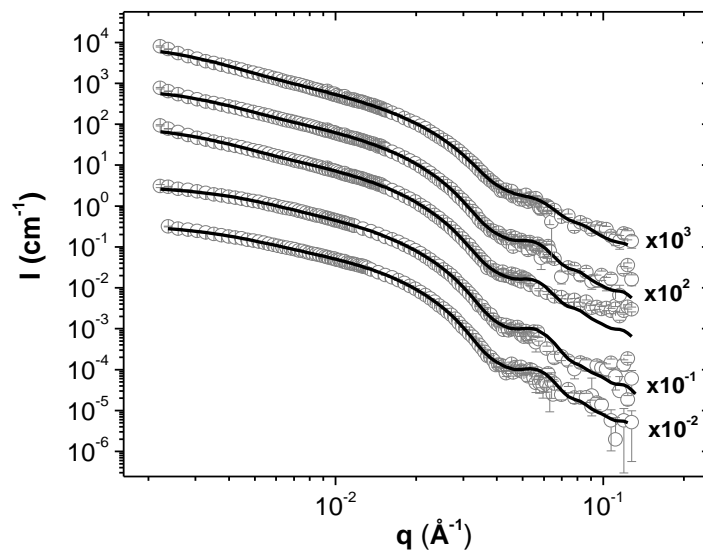


Figure 3: SANS intensities from PS-b-SCPI-b-PEO 1mg/ml in aqueous solutions of different conditions. From top to bottom: pH3/0M NaCl, pH7/0M NaCl, pH9/0M NaCl, pH7/0.1M NaCl and pH7/0.5M NaCl. Multiplication factors (as pointed in the figure) have been used for sake of clarity. The lines are fits to the experimental data.

We modelled our SANS data with a superposition of scattering from fractal aggregates and well-defined objects of spherical symmetry [17]. A single-component system i.e. well-defined objects of spherical symmetry were also tested and did not give fits of best quality. Additionally, the fitted sizes showed big discrepancies compared to the Light Scattering results. As in previous studies of self-assembling block copolymers in solution the structure of the well-defined objects has been fitted with models of increasing complexity until the best fit was obtained [18, 19]. Assuming spherical symmetry, homogeneous spheres, core-shell models with uniform densities,

core-shell models with multiple concentric shells and core-shell models with a uniform core and a corona with varying density are examples of models of increasing complexity. Polydispersity in sizes and densities can also be introduced to all the above models. The model that best fitted our data was a monodisperse core-shell-shell model with a uniform core and two concentric shells with varying density. As a model's complexity increases, so does the number of the fitting parameters, but when this is accompanied by significant improvement in the quality of the fits, then the increased number of fitting parameters is justified [19].

The scattered intensity was modelled by equation 3 for both triblock terpolymer systems.

$$I(q) = I^{frac}(q) + I^{mic}(q) \quad (3)$$

Where I^{frac} is the scattered intensity from fractal aggregates. This contribution is modelled[20] by a unified Guinier/power-law (equation 4)

$$I^{frac}(q) = G \cdot \exp\left(-\frac{q^2 R_{g,frac}^2}{3}\right) + \frac{B}{q^d} \left[\operatorname{erf}\left(-\frac{q R_{g,frac}}{\sqrt{6}}\right) \right] \quad (4)$$

The term $G \cdot \exp\left(-\frac{q^2 R_{g,frac}^2}{3}\right)$ is the Guinier regime behavior and the term $\frac{B}{q^d}$ is the high- q power-law behavior of the fractal aggregates' scattering. The $\operatorname{erf}\left(-\frac{q R_{g,frac}}{\sqrt{6}}\right)$ term provides a smooth transition[21] between the two regimes. $R_{g,frac}$ and d are the radius of gyration and the fractal exponent of the fractal aggregates respectively. G is the pre-exponential factor and is given by $G = N_{frac} \cdot \Delta\rho_{frac}^2 \cdot V_{frac}^2$, where N_{frac} is the number density of fractal aggregates in solution, $\Delta\rho_{frac}$ is the contrast in neutron scattering length density between solvent and

aggregates and V_{frac} their volume. The prefactor of the power-law is calculated by $B = \frac{G \cdot d}{R_{g,frac}^d}$.

$\left[\frac{6d^2}{(2+d)(2+2d)} \right]^{d/2} \Gamma\left(\frac{d}{2}\right)$ and Γ refers to the gamma function.

I^{mic} is the scattered intensity from the well-defined objects i.e. core-shell-shell spherical objects. In this kind of geometry the scattered intensity[22] is given by equation 5.

$$I^{mic}(q) = N_{mic} \cdot \left\{ 4\pi \int_0^\infty (\rho(r) - \rho_{D_2O}) r^2 \frac{\sin qr}{qr} dr \right\}^2 \quad (5)$$

Where N_{mic} is the number density of objects in solution.

The neutron scattering-length-density (ρ) as a function of the radial distance (r) is written as in equation 6. Where ρ_{core} is the uniform scattering-length-density of the core, $\rho_{in}(r)$ and $\rho_{out}(r)$ are the varying scattering-length-densities of the inner and outer shells respectively and ρ_{D_2O} is the scattering-length-density of the solvent. The radii R_c , R_{in} and R_{out} are the radius of the core, the inner shell and the outer shell respectively.

$$\rho(r) = \begin{cases} \rho_{core} & \text{for } 0 \leq r < R_c \\ \rho_{in}(r) & \text{for } R_c \leq r < R_{in} \\ \rho_{out}(r) & \text{for } R_{in} \leq r < R_{out} \\ 0 & \text{for } r \geq R_{out} \end{cases} \quad (6)$$

Figure 4 presents the most plausible morphology of the well-defined objects. They are core-corona micellar nanoparticles and this is the reason why the corresponding scattered intensity is denoted as I^{mic} . For the SCPI-b-PS-b-PEO triblock terpolymer a solid core is expected to form because of the hydrophobic nature of PS which drives self-assembly between triblock chains. Since the PS-blocks are the middle blocks of the chains two tails from each PS-block are expected to extend to solution. These two blocks i.e. SCPI and PEO are both hydrophilic. The SCPI block contains almost twice more monomers than the PEO block and hence it is expected

to extend further into solution compared to the PEO block. This extension of the SCPI is additionally reinforced by the fact that SCPI is a charged polymer compared to PEO which is a neutral water-soluble polymer. This conformation produces an inner shell containing both PEO and SCPI segments (mixed brush) and an outer shell containing only SCPI segments and explains the discontinuous scattering-length-density profile of equation 5. Both the hydrophilic components extend to solution because of the SCPI/PEO and PEO/PEO steric interactions and SCPI/SCPI electrostatic repulsions that conventionally induce the formation of neutral or charged spherical macromolecular brushes[23].

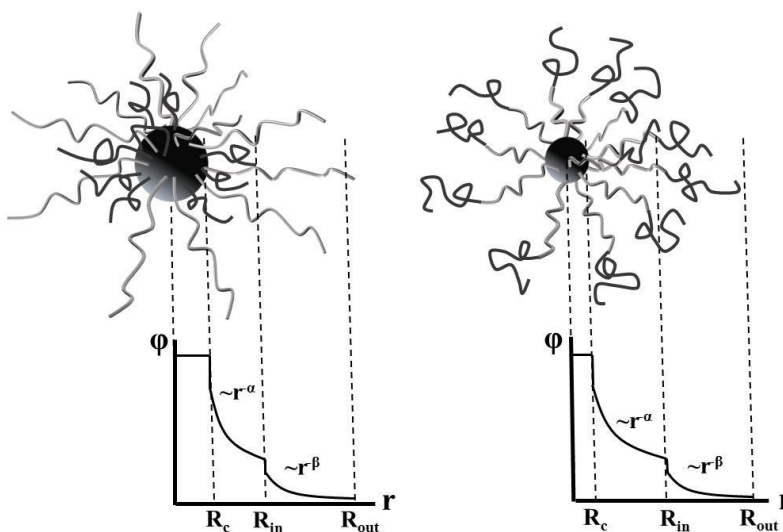


Figure 4: Proposed structure of the micellar nanoparticles formed by SCPI-b-PS-b-PEO (left) and PS-b-SCPI-b-PEO (right) triblock terpolymers in aqueous solutions. PS-cores, PEO-blocks and SCPI-blocks are represented by spheres, black chains and grey chains respectively. The respective segmental volume fraction as a function of the radial distance is also shown.

Consequently, the scattering length densities of equation 6 are given by $\rho_{core} = \rho_{PS}$, $\rho_{in}(r) = \varphi_{SCPI}^{in}(r) \cdot \rho_{SCPI} + \varphi_{PEO}^{in}(r) \cdot \rho_{PEO} + (1 - \varphi_{SCPI}^{in}(r) - \varphi_{PEO}^{in}(r)) \cdot \rho_{D_2O}$ and $\rho_{out}(r) = \varphi_{SCPI}^{out}(r) \cdot \rho_{SCPI} + (1 - \varphi_{SCPI}^{out}(r)) \cdot \rho_{D_2O}$. Where ρ_{PS} , ρ_{SCPI} and ρ_{PEO} are the neutron scattering-length-densities of the three blocks; $\varphi_{SCPI}^{in}(r)$ and $\varphi_{PEO}^{in}(r)$ are the volume fractions of SCPI and PEO segments respectively in the inner shell. These volume fractions were modeled by power-laws as in equation 7. The use of power-laws is a common practice for neutral and charged macromolecular spherical brushes[24] since it is predicted by scaling theories[25, 26]. The exponent (α) for the inner-shell is taken to be the same for the two-blocks not because they are expected to be so, since they are chains of different nature (neutral vs polyelectrolyte chains) but because the quality of the fits did not become better choosing two different exponents as fitting parameters. In other words, from our data we cannot resolve possible differences in the two exponents.

$$\varphi_{SCPI \text{ or } PEO}^{in}(r) = \varphi_{0,in}^{SCPI \text{ or } PEO} \cdot \left(\frac{r}{R_c}\right)^{-\alpha} \quad (7)$$

Where $\varphi_{0,in}^{SCPI \text{ or } PEO}$ is the volume fraction at the PS/solution interface for SCPI or PEO segments respectively.

The volume fraction in the outer shell is given by equation 8 with a power-law exponent β and a volume fraction $\varphi_{0,out}^{SCPI}$ at the boundary between inner and outer shell.

$$\varphi_{SCPI}^{out}(r) = \varphi_{0,out}^{SCPI} \cdot \left(\frac{r}{R_{in}}\right)^{-\beta} \quad (8)$$

The PS-b-SCPI-b-PEO core-shell-shell particles are expected to have a hydrophobic PS-core, formed by the self-assembly of the PS-segments that are the end-blocks of the triblock chains.

SCPI blocks will emerge from the PS-solution interface and sequentially PEO blocks will extend further into solution (figure 4). A discontinuous scattering-length-density profile in the corona is due to the difference in the volume between PEO and SCPI monomers and also because of the different type of the two brushes. The scattering-length-densities of equation 6 will be given by $\rho_{core} = \rho_{PS}$, $\rho_{in}(r) = \varphi_{SCPI}^{in}(r) \cdot \rho_{SCPI} + (1 - \varphi_{SCPI}^{in}(r)) \cdot \rho_{D_2O}$ and $\rho_{out}(r) = \varphi_{PEO}^{out}(r) \cdot \rho_{PEO} + (1 - \varphi_{PEO}^{out}(r)) \cdot \rho_{D_2O}$. The corresponding volume fraction profiles are given by equations 9 and 10.

$$\varphi_{SCPI}^{in}(r) = \varphi_{0,in}^{SCPI} \cdot \left(\frac{r}{R_c}\right)^{-\alpha} \quad (9)$$

$$\varphi_{PEO}^{out}(r) = \varphi_{0,out}^{PEO} \cdot \left(\frac{r}{R_{in}}\right)^{-\beta} \quad (10)$$

Where $\varphi_{0,in}^{SCPI}$ and $\varphi_{0,out}^{PEO}$ are the volume fraction of the SCPI at the PS/solution interface and PEO at the boundary between inner and outer shell respectively. The volume fraction power-law exponents are denoted again as α and β .

The quality of the fits and the separate contributions to the scattered intensities are shown, together with the corresponding volume fraction profiles, in figure 5, for the two systems at pH7 with no added salt.

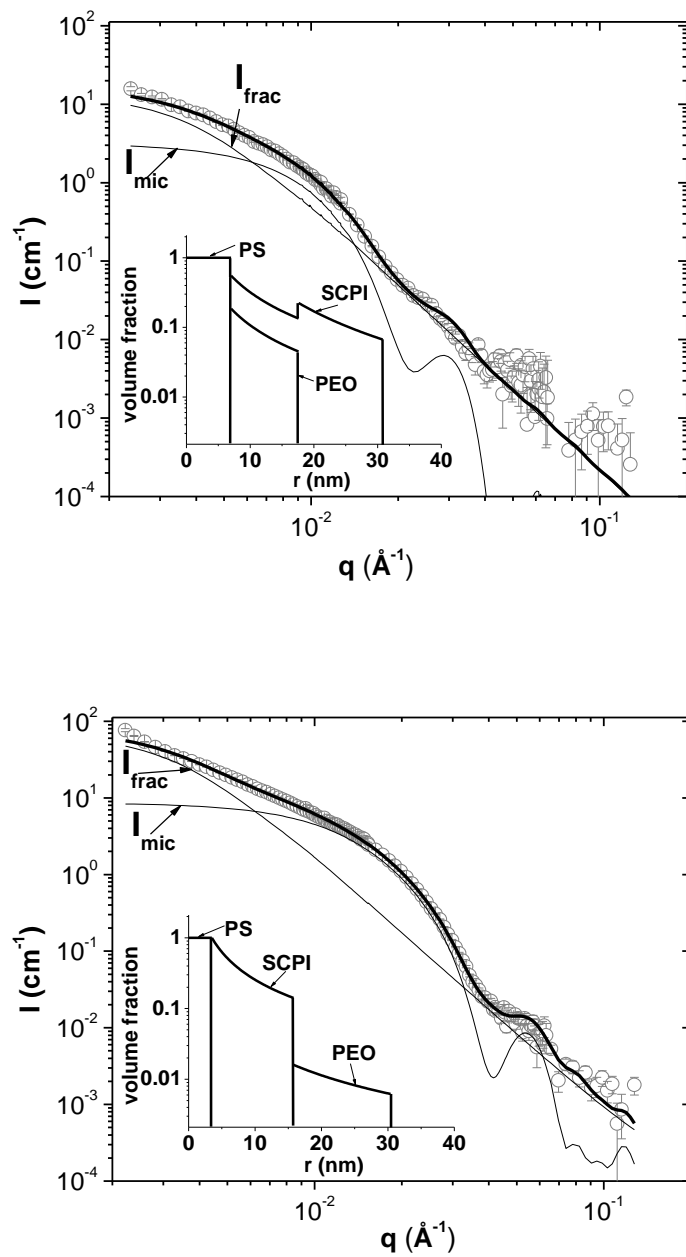


Figure 5: Fitted scattered intensities for SCPI-b-PS-b-PEO (top) and PS-b-SCPI-b-PEO (bottom) in aqueous solutions 1mg/ml at pH7 with no added salt. The separate contributions of micellar and fractal aggregates are shown. The corresponding volume fraction profiles of the micellar aggregates are also presented.

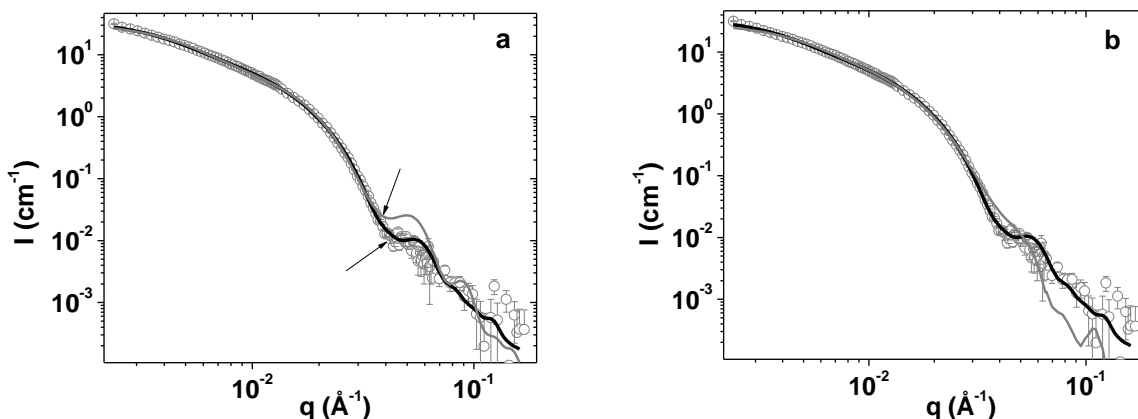


Figure 6: (a) Best fits (lines) with fractal aggregates, coexisting with core-shell (grey) and core-shell-shell models (black) for the micellar form factor (turning points highlighted by arrows). (b) Best fits (lines) with fractal aggregates, coexisting with cylindrical (grey) and spherical core-shell-shell (black) models for the micellar form factor. The experimental data are from PS-b-SCPI-b-PEO at pH7 and 0.5M added salt.

In figure 6a the used spherical core-shell-shell model is compared to a spherical core-shell model for the micelles. The form factor of aggregates is again added to the total scattered intensity. It is shown that when a spherical model with lower number of shells is used, the turning point cannot follow the experimentally obtained data. In figure 6b the spherical core-shell-shell model is compared to a cylinder with two coaxial shells. The fitting curve does not follow the trend of the data for $q > 0.03 \cdot \text{\AA}^{-1}$ in the case of the cylindrical model. We have also tested and rejected ellipsoidal models in the same way. The cylindrical core-shell-shell and spherical core-shell models are not under any constraint as the spherical core-shell-shell models

for number of block monomers and block sequence as the core-shell-shell models (see discussions in sections 3.2 and 3.3).

The three parameters of the fractal aggregates determine the scattering curves at low- q . There the zero- q scattering strength and R_g (of fractals) are determined independently since the Guinier-to-power law transition is clear. At intermediate- q and high- q the fractal scattering is a straight line (power-law) which does not contribute to the specific features (although weak ones) of the curves. In this regime the micellar scattering determines the features. In figure 6 we give proof that less complex models or models of high complexity but different geometry do not fit well. Of course a high number of fitting parameters brings the question of their mutual dependency. We have to keep in mind that since we are forced to go from a core-shell model to a core-shell-shell model it means that the system “needs” one more independent length scale to be introduced. This intuitively points that the thickness and concentration of the new shell will be independent from the other parameters. Using a uniform shell does not give a good fit. This in a similar manner renders the exponent of the varying density profile adequately independent.

Finally, Hessian matrix (H) calculations for our nonlinear optimization problem, with the second derivatives of χ^2 , $H_{ij} = \frac{\partial^2 \chi^2}{\partial p_i \partial p_j}$ around the optimal values (minimum of χ^2) of the fitted parameters p_i have been made. Where χ^2 is the chi-squared function under minimization, $\chi^2 = \sum_{i=1}^N \left[\frac{1}{\sigma_i} \left(I^{th}(q_i, p_{1,2,\dots,M}) - I^{exp}(q_i) \right) \right]^2$, $p_{1,2,\dots,M}$ are the fitting parameters, I^{th} are the theoretically calculated and I^{exp} the experimentally obtained scattered intensities with their experimental uncertainty σ_i . Inverting the matrix, $R_{ij} \sim H_{ij}^{-1}$ we obtain the correlation

coefficients by $r_{ij} = \frac{R_{ij}}{\sqrt{R_{ii} \cdot R_{jj}}}$. In all cases the coefficients are within acceptable limits, proving the reliability of the used models (see Supporting Material for more details).

3.2 Morphology of aggregates in the SCPI-b-PS-b-PEO system

The parameters extracted from the SANS data on the SCPI-b-PS-b-PEO triblock terpolymers are shown in table 1. The fitting parameters for the fractal aggregates are G , $R_{g,frac}$ and d . The fitting parameters for the micellar objects are N_{mic} , R_c , R_{in} , R_{out} , α and β . The aggregation number of micelles (N^{mic}) i.e. the number of macromolecular chains within one micelle is calculated[15] assuming that the core is solid PS, consisting of collapsed PS-blocks with molecular weight $M_{PS-BLOCK}$ each, by $N^{mic} = \frac{4}{3}\pi R_c^3 d_{PS} \frac{N_A}{M_{PS-BLOCK}}$. Where N_A is the

Avogadro's number and d_{PS} is the mass density of PS. The volume fractions $\varphi_{0,in}^{SCPI}$, $\varphi_{0,out}^{SCPI}$ and $\varphi_{0,in}^{PEO}$ are calculated by the constant that the total amount of each block within a micelle must

correspond to the micellar aggregation number due to the fixed connectivity of the terpolymer

chains i.e. $N^{mic} = d_{SCPI \text{ or } PEO} \cdot \frac{N_A}{M_{SCPI \text{ or } PEO-BLOCK}} \cdot 4\pi \int_0^{R_{out}} r^2 \varphi_{SCPI \text{ or } PEO}(r) dr$. Where

$d_{SCPI \text{ or } PEO}$ and $M_{SCPI \text{ or } PEO-BLOCK}$ are the respective densities and molecular weights of the SCPI and PEO blocks. Since SCPI is contained in two shells there is an additional fitting parameter which defines the percentage of SCPI segments in the outer layer (% SCPI out, table

1). The radius of gyration of the micellar nanoparticles is calculated by $R_{g,mic}^2 = \frac{\int_0^{R_{out}} r^4 \varphi(r) dr}{\int_0^{R_{out}} r^2 \varphi(r) dr}$,

where $\varphi(r)$ is the segments' volume fraction independently of the kind of block. This calculation is expected to provide a generally different values for the radius of gyration compared to the ones measured by SANS, where the average is weighted by the neutron scattering-length-density

which is different for the different blocks. We use the volume fraction weighted average since we will compare this value with the Light Scattering data. In SLS the average corresponds to the distribution of the refractive index increment which does not defer remarkably for the three blocks involved in this study.

Table 1: Fitted and calculated parameters for SCPI-b-PS-b-PEO 1mg/ml in aqueous solutions at different solution conditions from SANS and LS.

Parameters/Conditions	pH3/0M	pH7/0M	pH9/0M	pH7/0.1M	pH7/0.5M
R_c (nm)	7.1±0.3	7.0±0.3	7.4±0.3	7.3±0.3	7.1±0.3
R_{in} (nm)	17.6±0.6	17.6±0.6	17.9±0.6	18.2±0.6	16.8±0.6
R_{out} (nm)	30.7±0.8	30.8±0.8	31.5±0.8	33.4±0.8	31.0±0.8
$R_{g,mic}$ (nm)	13.5±0.4	13.8±0.4	14.1±0.4	14.6±0.4	14.3±0.4
$\phi_{0,in}^{SCPI}$	$(7.4±0.6) \cdot 10^{-1}$	$(5.5±0.6) \cdot 10^{-1}$	$(7.7±0.6) \cdot 10^{-1}$	$(5.5±0.6) \cdot 10^{-1}$	$(5.0±0.6) \cdot 10^{-1}$
ϕ_0^{PEO}	$(1.9±0.3) \cdot 10^{-1}$	$(1.9±0.3) \cdot 10^{-1}$	$(2.0±0.3) \cdot 10^{-1}$	$(1.6±0.3) \cdot 10^{-1}$	$(1.7±0.3) \cdot 10^{-1}$
$\phi_{0,out}^{SCPI}$	$(2.0±0.6) \cdot 10^{-1}$	$(2.2±0.6) \cdot 10^{-1}$	$(2.1±0.6) \cdot 10^{-1}$	$(2.0±0.6) \cdot 10^{-1}$	$(2.2±0.6) \cdot 10^{-1}$
α	1.5±0.1	1.5±0.1	1.6±0.1	1.3±0.1	1.2±0.1
β	2.1±0.1	2.2±0.1	2.0±0.1	2.2±0.1	1.9±0.1
N^{mic}	180±10	170±10	200±10	190±10	170±10
%SCPI out	61±5	70±5	62±5	66±5	70±5
$I_0^{mic}(cm^{-1})$	17.8±0.5	3.2±0.3	14.8±0.4	1.5±0.1	9.6±0.4
$G(cm^{-1})$	26±1	14±1	63±1	9±1	46±1
$R_{g,frac}$ (nm)	37±4	45±4	47±4	46±4	50±4
d	3.3±0.2	3.4±0.2	3.5±0.2	3.4±0.2	3.4±0.2
N^{frac}	90±5	39±5	230±30	28±3	150±10
weight % mNPs	26±3	4.9±0.4	21±3	2.3±0.2	15±2
number % mNPs	15±1	1.2±0.2	23±4	0.3±0.02	14±2

$R_h (nm)$	40±3	47±3	47±3	43±3	59±3
$R_{g,SLS} (nm)$	35±2	46±2	46±2	39±2	58±2
$R_{g,app} (nm)$	30±2	41±2	43±2	43±2	46±2
N_{SLS}^{agg}	390±20	270±10	260±10	490±20	720±40
N^{app}	110±10	46±4	220±10	32±3	150±10

The forward scattered intensity due to micelles is given by $I_0^{mic} = N_{mic} \cdot \left\{ 4\pi \int_0^\infty (\rho(r) - \rho_{D_2O}) r^2 dr \right\}^2$ which can alternatively be written as $I_0^{mic} = \frac{c_{mic} \cdot N^{mic}}{N_A \cdot M} \cdot \left(\sum_i \frac{M_i}{d_i} \cdot (\rho_i - \rho_{D_2O}) \right)^2$, The summation is over the three blocks, d_i , M_i and ρ_i are the corresponding mass density, neutron scattering-length-density and molecular weight and M is the total molecular weight of one triblock chain. The solution mass concentration of micelles (c_{mic}) can be calculated in this way.

In a similar manner the forward scattering of fractal aggregates is written as $G = \frac{c_{frac} \cdot N^{frac}}{N_A \cdot M} \cdot$

$\left(\sum_i \frac{M_i}{d_i} \cdot (\rho_i - \rho_{D_2O}) \right)^2$. Since I_0^{mic} and G are experimentally determined, the ratio $\frac{c_{frac} \cdot N^{frac}}{c_{mic} \cdot N^{mic}} =$

$\frac{G}{I_0^{mic}}$ yields the number of macromolecular chains (N^{frac}) within one fractal aggregate taking into

account that $c_{frac} + c_{mic} = 1mg/ml$. Consequently, the weight (

weight % mNPs = $100 \cdot \frac{c_{mic}}{c_{mic} + c_{frac}}$) and number (

number % mNPs = $100 \cdot \frac{c_{mic}/N^{mic}}{c_{mic}/N^{mic} + c_{frac}/N^{frac}}$) percentage of micellar nanoparticles over the whole

population of micellar and fractal aggregates can be obtained (table 1).

The radius of gyration of a PEO block of molecular weight M in water can be estimated [27] by $R_g \approx 0.0215 \cdot M^{0.583} nm$. In the case of SCPI-b-PS-b-PEO this yields to $R_g \approx 4nm$ for an unperturbed PEO block. The average distance between grafting points on the PS/solution

interface ($s \approx \left(\frac{2N^{mic}}{4\pi R_c^2}\right)^{-1/2}$) is about $1nm$ (for all solution conditions) which means that there is a high degree of overlapping of PEO-blocks with other PEO-blocks or SCPI-blocks on the PS/solution interface. The thickness of the shell is $10nm$ which is compatible with some possible stretching of the PEO blocks due to steric repulsions. The SCPI segments within this shell are 30-40% of the total amount of SCPI segments. Since this is a polyelectrolyte chain, we can assume that the conformation of its charged components is stretched and this way this percentage corresponds to a continuous sub-block of the chain. The radius of gyration of an imaginary self-avoiding chain of SCPI can be calculated by $R_g \approx 0.0135 \cdot M^{0.61}nm$, which is an equation experimentally obtained for polyisoprene (PI) in a good solvent[28]. This yields to $R_g \approx 3nm$ in the inner layer which proves the stretching of the SCPI chains. The scaling exponent α of the volume fraction profile is 1.5 which is near $4/3$, the one of neutral polymer spherical brushes[29]. In the mixed brush, this is anticipated to be an effective scaling exponent since it describes both charged and neutral blocks. Additionally a possible collapsing of monomers or parts of SCPI blocks on the PS-core could produce loops of SCPI segments that would decrease the exponent from the polyelectrolyte brush scaling; where 2 is the expected value[30]. The high values of the volume fraction of $\varphi_{0,in}^{SCPI}$ (table 1) supports this explanation. A similar effect has been observed in the past on a similar system of diblock copolymer micellar nanoparticles[18] formed by PS-b-SCPI. The collapsing can be caused by the inherent hydrophobic nature of the SCPI backbone followed by a condensation of the counter ions of the collapsing segments and also by the presence of unmodified hydrophobic isoprene monomeric units. A possible collapsing would reduce the effective charged polyelectrolyte segments of the SCPI blocks which shows that their actual stretching is even higher than the one mentioned when we compare with the unperturbed R_g .

The outer shell, which contains solely SCPI segments, has a thickness of $13nm$ and the expected unperturbed size of these SCPI blocks is $R_g \approx 3nm$. This is a clear case of stretched chains. The scaling exponent in this purely polyelectrolyte brush is 2 as expected. The “anchoring” distance ($s \approx \left(\frac{N^{mic}}{4\pi R_{in}^2}\right)^{-1/2}$) on the inner/outer shell boundary is $4nm$.

The conformation of the SCPI-b-PS-b-PEO micellar nanoparticles is not affected by the bulk solution conditions i.e. pH and ionic strength. This is in accordance with osmotic polyelectrolyte brush behavior found for brushes with high counter ion content[29]. The pH changes affect the weakly charged COOH groups. Still, the presence of strongly charged SO₃ groups is proved to provide the brushes with enough counter ions. The PEO blocks are not expected to be affected appreciably by pH or salt.

The SCPI-b-PS-b-PEO micellar nanoparticles coexist with fractal aggregates which dominate the population (75-85% both in weight and number, table 1). Formation of fractal aggregates is possibly due to the hydrophobic inherent nature of the SCPI backbone that causes random inter-chain SCPI/SCPI and SCPI/PS contacts which lead to clustering of micelles in fractal aggregates. The radius of gyration of the fractal aggregates ($\sim 40nm$) is significantly higher than the one of the micelles ($\sim 14nm$). The fractal aggregates scatter neutrons as rough surface fractals[31] with characteristic exponent $d \approx 3.4$ (table 1). The size of the fractal aggregates does not seem to depend strongly on the solution conditions ($R_{g,frac} \approx 40 - 50nm$) except from the case of pH3 with no added salt where it is somewhat lower than the rest highlighting a possible collapse of SCPI. This reflects the increased hydrophobic nature of the SCPI segments caused by the neutralization of the COOH groups at low pH. Additionally, at low pH, it is well known that hydrogen bonding between the ether groups of PEO and the carboxyl groups of SCPI is formed

which leads to complexation and even to phase separation [32]. This effect could enhance the intermicellar bridges and the resulting phase separation. The aggregates's size is virtually insensitive to the salt content maybe because of the high osmotic pressure of the counterions in their interior of the fractal aggregates of interconnected micelles as found for polyelectrolyte microgels [33].

The aggregation number ($N^{frac} \approx 30 - 300$) shows large fluctuations, especially for the cases of pH7/0M and pH7/0.1M NaCl, with the solution conditions, while $R_{g,frac}$ is fairly constant. In these two cases the mass content in micellar nanoparticles, which is absolutely determined by the experiment, is very low (table 1) and corresponding N^{frac} values are low compared to the ones for the rest of the conditions. Since we believe that hydrophobic interaction is the main driving force of this aggregation we would not expect a breakage of the fractal aggregates with no significant change in $R_{g,frac}$. We hence conclude that in these two solutions and to some extent in the rest three there is some loss of material caused by filtration which makes the value of the total solution concentration and N^{frac} unreliable. This could mean that the virtual change in aggregation number is due to some change of the solution concentration caused by filtration. We can say that in the case of the SCPI-b-PS-b-PEO system there is a small percentage of the initial material that forms micelles, some undetermined amount of fractal aggregates of well-defined geometry and also some losses due to filtration.

3.3 Morphology of aggregates in the PS-b-SCPI-b-PEO system

The parameters extracted from the SANS data on the PS-b-SCPI-b-PEO triblock terpolymers are shown in table 2. The fitting parameters for the fractal aggregates are again G , $R_{g,frac}$ and d . The fitting parameters for the micellar objects are N_{mic} , R_c , R_{in} , R_{out} , α and β . The aggregation

number of micelles N^{mic} the volume fractions $\varphi_{0,in}^{SCPI}$ and $\varphi_{0,out}^{PEO}$ and the rest of the parameters are calculated in a similar manner as in the case of SCPI-b-PS-b-PEO system except that now the inner shell consists solely of the SCPI blocks and the outer shell of the PEO blocks. This of course implies the assumption that the PEO segments do not fold back into the inner shell.

The unperturbed radius of gyration of the PEO blocks of PS-b-SCPI-b-PEO in water is $R_g \approx 8nm$ whereas the thickness of the outer layer is $15nm$ (table 2) pointing to a quasi-unperturbed mushroom-like configuration of the PEO-blocks. The average distance between “grafting points” on the SCPI/PEO shell boundary ($s \approx \left(\frac{N^{mic}}{4\pi R_{in}^2} \right)^{-1/2}$) is about $10nm$ i.e. there is a low degree of overlapping between PEO-blocks which is nevertheless not enough to cause significant stretching. The scaling exponent $\beta \approx 1.4$ is reminiscent of the neutral brush exponent. The SCPI blocks contained in the inner shell would have an unperturbed self-avoiding-walk of size $R_g \approx 6nm$. The anchoring distance in this case is $2nm$ and the thickness of the layer is $12nm$. The anchoring distance and polyelectrolyte nature indicate high stretching in contrast with the observed shell thickness. This leads us to conclude again that collapsing of SCPI segments onto the PS core occurs. The scaling exponent $\alpha \approx 1.3$ and the high volume fraction of SCPI at the core/solution interface (almost 100%) corroborate with this observation.

Table 2: Fitted and calculated parameters for PS-b-SCPI-b-PEO 1mg/ml in aqueous solutions at different solution conditions from SANS and LS.

Parameters/Conditions	pH3/0M NaCl	pH7/0M NaCl	pH9/0M NaCl	pH7/0.1M NaCl	pH7/0.5M NaCl
R_c (nm)	3.3±0.1	3.4±0.1	3.5±0.1	3.2±0.1	3.4±0.1

$R_{in} (nm)$	15.3±0.5	15.8±0.5	15.9±0.5	15.6±0.5	15.5±0.5
$R_{out} (nm)$	30.0±0.8	30.4±0.8	30.6±0.8	30.5±0.8	30.5±0.8
$R_{g,mic} (nm)$	6.6±0.2	6.8±0.2	6.9±0.2	6.4±0.2	6.8±0.2
φ_0^{SCPI}	1.00±0.01	1.00±0.01	1.00±0.01	0.98±0.01	0.99±0.01
φ_0^{PEO}	(1.5±0.2)×10 ⁻²	(1.6±0.2)×10 ⁻²	(1.6±0.2)×10 ⁻²	(1.1±0.2)×10 ⁻²	(1.5±0.2)×10 ⁻²
α	1.5±0.1	1.3±0.1	1.3±0.1	1.3±0.1	1.2±0.1
β	1.4±0.1	1.5±0.1	1.5±0.1	1.1±0.1	1.5±0.1
N^{mic}	23±2	25±2	26±2	21±2	24±2
$I_0^{mic} (cm^{-1})$	6.5±0.1	9.2±0.1	10.2±0.1	6.2±0.1	7.1±0.1
$G (cm^{-1})$	91±1	74±1	88±1	26±1	29±1
$R_{g,frac} (nm)$	57±3	52±3	53±3	38±3	41±3
d	3.0±0.1	3.2±0.1	3.2±0.1	3.5±0.1	3.3±0.1
N^{frac}	230±30	190±30	320±50	70±10	80±10
<i>weight % NPs</i>	42±3	49±3	58±3	47±3	45±3
<i>number % NPs</i>	88±5	88±5	95±5	77±5	73±5
$R_h (nm)$	30±2	31±2	30±2	31±2	30±2
$R_{g,SLS} (nm)$	32±1	32±1	32±1	33±1	32±1
$R_{g,app} (nm)$	56±2	49±2	50±2	34±2	37±2
N_{SLS}^{agg}	48±2	49±2	49±2	48±2	49±2
N^{app}	144±10	110±10	146±10	50±5	54±5

The morphology of the PS-b-SCPI-b-PEO micellar nanoparticles is unaltered upon addition of salt or change of pH (within experimental error) showing an osmotic brush behavior as in the

previous system. Their aggregation number is lower than the one of the SCPI-b-PS-b-PEO micellar nanoparticles possibly due to their lower relative content in PS. The PS-b-SCPI-b-PEO micellar nanoparticles ($R_{g,mic} \approx 7nm.$) coexist with larger fractal aggregates ($R_{g,frac} \approx 40 - 60nm$). The fractal aggregates' fractal dimension ($d \approx 3.2$) is in the limit between rough surface fractals and mass fractals [34]. Their aggregation number (N^{frac}) is significantly higher than the one of the micellar nanoparticles (N^{mic}). The percentage of micellar nanoparticles in solution though, is $\sim 50\%$ in weight and $\sim 80 - 90\%$ in number which means that a high content of micellar nanoparticles is available in this system. It is seemingly easier for this system with the highly hydrophobic block in the end of the macromolecular chain to form well-defined objects compared to the one with the PS block in the middle which shows strong tendency to cause intermicellar aggregation. The PEO outer shell appears to give better stability to the PS-b-SCPI-b-PEO system in contrast to the SCPI-b-PS-b-PEO system where the SCPI segments in the corona increase the tendency for intermicellar interactions. Possibly the aforementioned PEO/SCPI hydrogen bonding and SCPI/SCPI hydrophobic attractions are reduced by the presence of PEO in the outer layer. There is a significant drop in N^{frac} when salt is added to the solutions with a simultaneous though less intense drop in $R_{g,frac}$. At the same time the number percentage of fractal aggregates increases while their weight percentage remains unaltered. All these point to breakage of fractal aggregates into smaller fragments. This breakage of the fractal aggregates by addition of salt could be explained by a possible shrinkage of SCPI chains that causes the intermicellar bridges within the fractal aggregates to break.

3.4 Light Scattering Measurements

Parameters extracted from LS from both systems are incorporated in tables 1 and 2. The radius of gyration ($R_{g,SLS}$) and aggregation number (N_{SLS}^{agg}) are obtained by the Zimm representation of the LS data at a single concentration (1mg/ml). Collecting field autocorrelation functions and performing the CONTIN analysis a single-peak distribution curves are obtained (figure 7). The diffusion coefficient (D) was obtained by the slope of the $\Gamma(q) = D \cdot q^2$ curves (figure 8). The hydrodynamic radius (R_h) is obtained by equation 3.

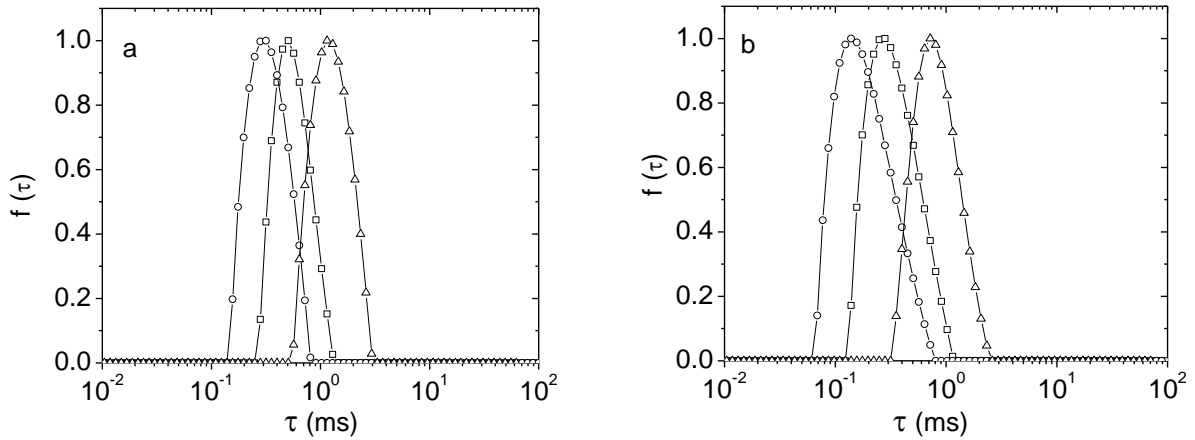


Figure 7: Distribution of relaxation times obtained by CONTIN analysis for SCPI-b-PS-b-PEO (a) and PS-b-SCPI-b-PEO (b), for three different angles 45° (triangles), 90° (squares) and 135° (circles) at pH7 with no added salt.

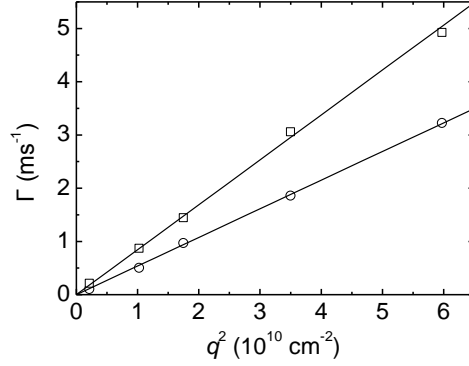


Figure 8: Scattering-wave-vector dependence of the main relaxation rate for SCPI-b-PS-b-PEO (circles) and PS-b-SCPI-b-PEO (squares) in pH 7 with no added salt. Linear fits to the data (straight lines) are also included.

In a two-component system a superposition of the scattering from each individual component is measured. SLS exploits larger length scales than SANS since its q -regime is from 0.0004 to 0.003 \AA^{-1} (for the angle range used in this study). This way the information in length scales relative to SANS is lost and in our case the observed length-scales fall well inside SANS regime. In other words the Guinier regime for both species (fractal and micellar aggregates) is observed by SLS. The scattered intensity in the SLS, expected by the findings of SANS can be written in the Guinier/Zimm approximation for low- q . Based on the parameters extracted from SANS, the combination from the two separate components is given by equation 11.

$$I(q) = G \cdot \left(1 - \frac{q^2 R_{g,frac}^2}{3}\right) + I_0^{mic} \cdot \left(1 - \frac{q^2 R_{g,mic}^2}{3}\right) \quad (11)$$

Equation 11 leads to an apparent radius of gyration expected to be observed by SLS

$$R_{g,app}^2 = \frac{c_{frac} \cdot N^{frac} \cdot R_{g,frac}^2 + c_{mic} \cdot N^{mic} \cdot R_{g,mic}^2}{c_{frac} \cdot N^{frac} + c_{mic} \cdot N^{mic}} \quad (12)$$

Additionally the expected aggregation numbers of the observed particles by SLS is written as in equation (13).

$$N^{app} = \frac{c_{frac} \cdot N^{frac} + c_{mic} \cdot N^{mic}}{c_{frac} + c_{mic}} \quad (13)$$

In terms of gyration radii the agreement is very good for the SCPI-b-PS-b-PEO system (table 1) i.e. $R_{g,app} \approx R_{g,SLS}$ for all solution conditions. This is because the fractal aggregates determine the apparent radius ($R_{g,app}$ is very near to $R_{g,frac}$) in D₂O (SANS) and because the proportions of micelles, fractals and amount lost by filtration are apparently not much different in H₂O compared to D₂O. DLS gives R_h values that are higher than the micellar radii R_{out} which is caused by the dominance of fractal aggregates in scattering. The breadth of the CONTIN distribution functions (figure 7a) is compatible with any possible polydispersity of the aggregates or the presence of the small fraction of micelles that have a not much lower radius than the observed hydrodynamic radius. Finally, $R_{g,SLS}$ appears to show a lower value for pH3/0M NaCl compared to the rest of the solutions following the trend of the fractal aggregates found by SANS.

The PS-b-SCPI-b-PEO triblock terpolymer has a $R_{g,SLS}$ that is independent of solution conditions (table 2). This value is between $R_{g,app}$ and $R_{g,mic}$ showing that the percentage of fractal aggregates in H₂O is smaller than the one in D₂O or in other words, in H₂O there is a higher content in micelles. This is supported by the fact that the hydrodynamic radius agrees with the micellar radius R_{out} . Probably the weak contribution of the larger fractal aggregates is covered by the breadth of the distribution function of CONTIN (figure 7b). Similarly, the

aggregation number measured by SLS in H₂O (table 2) is between N_{app} and N_{mic} . The LS experiments do not show any sign of breakage of the fractal aggregates upon addition of salt.

4. CONCLUSIONS

In the present study two triblock terpolymers containing blocks of the same chemistry in different sequence were studied by SANS and LS. In both systems fractal and micellar aggregates were observed by SANS which proves its power due to length-scale of observation and scattering contrast. The micellar aggregates were well-defined core-shell-shell spherical objects, consistent with the well-known charged and neutral macromolecular spherical brushes. SANS quantitatively defined the aggregation number and percentages of the species in solution and also the characteristic dimensions involved in each kind of populations. The parameters extracted by SANS were used to successfully interpret the LS results, where average values are obtained since in the systems under study there is no possibility to distinguish between the two species. It is observed (as expected) that LS is very sensitive to the presence of fractal aggregates even at low contents. The PS-*b*-SCPI-*b*-PEO system provides solutions with a higher percentage in micellar nanoparticles. Micelles of both systems are stable in all solution conditions, whereas aggregates are breaking up at high salt contents in the PS-*b*-SCPI-*b*-PEO system. Fractal aggregates have possibly a network like structure that could be useful for drug loading and other relevant applications of similar amphiphilic block copolymer systems. In conclusion the amphiphilic triblock terpolymers aqueous solutions under study provide a ground for analysing systems containing several species of different morphologies and with possibly different physicochemical capabilities in order to evaluate their potential for drug loading and release.

5. ACKNOWLEDGEMENTS

The authors acknowledge financial support by the NANOMACRO 1129 project which is implemented in the framework of the Operational Program “Education and Life-long Learning” of the National Strategic Reference Program-NSRF (Action “ARISTEIA I”) and it is co-funded by the European Union (European Social Fund-ESF).

The SANS experiments have been supported by the European Commission under the 7th Framework Programme through the Key Action: Strengthening the European Research Area, Research Infrastructures. Contract no.: 226507 (NMI3). The work is based on experiments performed at the Jülich Centre for Neutron Science JCNS, Forschungszentrum Jülich, Germany.

REFERENCES

1. Stuart, M.A.C., et al., *Emerging applications of stimuli-responsive polymer materials*. Nat Mater, 2010. **9**(2): p. 101-113.
2. Miyata, K., R.J. Christie, and K. Kataoka, *Polymeric micelles for nano-scale drug delivery*. Reactive and Functional Polymers, 2011. **71**(3): p. 227-234.
3. Riess, G., *Micellization of block copolymers*. Progress in Polymer Science, 2003. **28**(7): p. 1107-1170.
4. Ballauff, M., *Spherical polyelectrolyte brushes*. Prog. Polym. Sci., 2007. **32**: p. 1135–1151.
5. Hadjichristidis, N., et al., *Linear and non-linear triblock terpolymers. Synthesis, self-assembly in selective solvents and in bulk*. Progress in Polymer Science, 2005. **30**(7): p. 725-782.
6. Kabanov, A. and S. Vinogradov, *Nanogels as Pharmaceutical Carriers*, in *Multifunctional Pharmaceutical Nanocarriers*, V. Torchilin, Editor. 2008, Springer New York. p. 67-80.
7. Ryu, J.-H., et al., *Self-Cross-Linked Polymer Nanogels: A Versatile Nanoscopic Drug Delivery Platform*. Journal of the American Chemical Society, 2010. **132**(48): p. 17227-17235.
8. Muller, F., et al., *Salt-induced contraction of polyelectrolyte brushes*. Journal of Physics: Condensed Matter, 2005. **17**(45): p. S3355.
9. Pispas, S., *Double Hydrophilic Block Copolymers of Sodium(2-sulfamate-3-carboxylate)isoprene and Ethylene Oxide*. J. Polym. Sci. Part A: Polym. Chem., 2006. **44**: p. 606-613.

10. Uchman, M., et al., *Multicompartment Nanoparticles Formed by a Heparin-Mimicking Block Terpolymer in Aqueous Solutions*. *Macromolecules*, 2009. **42**(15): p. 5605-5613.
11. Barker, J.G. and J.S. Pedersen, *Instrumental Smearing Effects in Radially Symmetric Small-Angle Neutron Scattering by Numerical and Analytical Methods*. *J. Appl. Crystallogr.*, 1995. **28**: p. 105-114.
12. Vad, T., et al., *Experimental determination of resolution function parameters from small-angle neutron scattering data of a colloidal SiO₂ dispersion*. *Journal of Applied Crystallography*, 2010. **43**(4): p. 686-692.
13. Chu, B., *Laser Light Scattering*. 2 ed. 1991, New York: Academic Press.
14. Uchman, M., et al., *pH-Dependent Self-Assembly of Polystyrene-block-Poly((sulfamate-carboxylate)isoprene) Copolymer in Aqueous Media*. *Langmuir*, 2008. **24**: p. 12017-12025.
15. Berne, B.J. and R. Pecora, *Dynamic Light Scattering, With Applications to Chemistry, Biology, and Physics*. 2000, Toronto: Dover.
16. Forster, S., et al., *Structure of Polyelectrolyte Block Copolymer Micelles*. *Macromolecules*, 2002. **35**: p. 4096-4105.
17. Papagiannopoulos, A., et al., *Thermoresponsive aggregation of PS–PNIPAM–PS triblock copolymer: A combined study of light scattering and small angle neutron scattering*. *European Polymer Journal*, 2014. **56**(0): p. 59-68.
18. Papagiannopoulos, A., et al., *Self-Assembled Nanoparticles from a Block Polyelectrolyte in Aqueous Media: Structural Characterization by SANS*. *The Journal of Physical Chemistry B*, 2010. **114**(22): p. 7482-7488.

19. Papagiannopoulos, A., et al., *Thermoresponsive transition of a PEO-b-PNIPAM copolymer: From hierarchical aggregates to well defined ellipsoidal vesicles*. *Polymer*, 2013. **54**(23): p. 6373-6380.
20. Beaucage, G., *Small-Angle Scattering from Polymeric Mass Fractals of Arbitrary Mass-Fractal Dimension*. *J. Appl. Crystallogr.*, 1996. **29**: p. 134-146.
21. Hammouda, B., *Analysis of the Beaucage model*. *Journal of Applied Crystallography*, 2010. **43**(6): p. 1474-1478.
22. Higgins, J.S. and H.C. Benoit, *Polymers and Neutron Scattering*. 1994: OUP.
23. Pincus, P., *Colloid Stabilization with Grafted Polyelectrolytes*. *Macromolecules*, 1991. **24**: p. 2912-2919.
24. Forster, S., E. Wenz, and P. Lindner, *Density Profile of Spherical Polymer Brushes*. *Phys. Rev. Lett.*, 1996. **77**: p. 95-98.
25. Forster, S., V.A. Abetz, and H.E. Muller, *Polyelectrolyte Block Copolymer Micelles*. *Adv Polym Sci*, 2004. **166**: p. 173-210.
26. Van Der Maarel, J.R.C., et al., *Salt induced contraction of polyelectrolyte diblock copolymer micelles*. *Langmuir*, 2000. **16**: p. 7510-7519.
27. Devanand, K. and J.C. Selser, *Asymptotic behavior and long-range interactions in aqueous solutions of poly(ethylene oxide)*. *Macromolecules*, 1991. **24**(22): p. 5943-5947.
28. Tsunashima, Y., et al., *Dilute solution properties of cis-polyisoprene in cyclohexane and 1,4-dioxane*. *Macromolecules*, 1988. **21**(4): p. 1107-1117.
29. Borisov, O.V. and E.B. Zhulina, *Effects of ionic strength and charge annealing in star-branched polyelectrolytes*. *Eur. Phys. J. B*, 1998. **4**: p. 205-217.

30. Klein Wolterink, J., et al., *Annealed Star-Branched Polyelectrolytes in Solution*. *Macromolecules*, 2002. **35**(24): p. 9176-9190.
31. Schaefer, D.W., et al., *Multilevel structure of reinforcing silica and carbon*. *Journal of Applied Crystallography*, 2000. **33**(3 Part 1): p. 587-591.
32. Khutoryanskiy, V.V. and G. Staikos, *Hydrogen-Bonded Interpolymer Complexes: Formation, Structure and Applications* 2009: World Scientific.
33. English, A.E., et al., *Equilibrium swelling properties of polyampholytic hydrogels*. *The Journal of Chemical Physics*, 1996. **104**(21): p. 8713-8720.
34. Schmidt, P., *Small-angle scattering studies of disordered, porous and fractal systems*. *Journal of Applied Crystallography*, 1991. **24**(5): p. 414-435.